energy and the position of each single photon is used for the analysis. Thus, in contrast to the 'multi-photon method', photons of a certain energy range can be selected where the analyzing power of the cross section is largest. In addition, correlations of position and energy of the Compton photons can be used to study the systematic precision of the polarization results.

3.2 The Laser Optics

Figure 10 shows an overview of the polarimeter layout. A 10 W argon ion laser provides a continuous, linearly polarized laser beam at the green line of 514 nm. A Pockels cell converts the polarization state to right (left) circularly polarized light with a switching frequency of about 90 Hz. A chopper which blocks the beam for 20 s once a minute is used for background measurement. A remotely controlled mirror system transports the laser beam down to the interaction point in the HERA tunnel. A doublet lens system with 14.5 m focal length focuses the beam onto the electron beam with a spot size of $\sigma \approx 600\ \mu m$. Most of the transport line is under vacuum to reduce deflections by air turbulence. For mechanical simplicity, all mirrors are outside the vacuum. Position sensitive photo-diodes behind the mirrors, which detect the small fraction of the transmitted light, are used as position monitors.

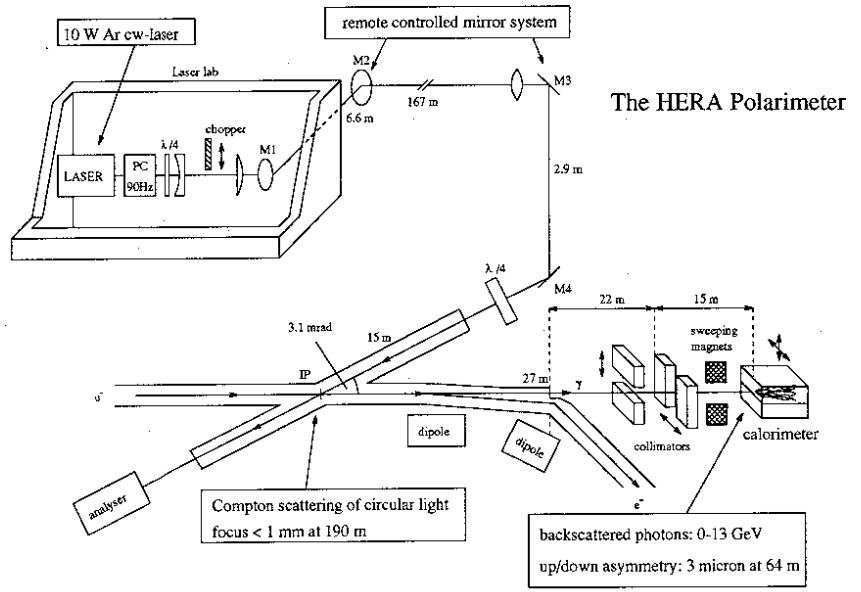

Figure 10: Layout of the HERA polarimeter. A laser beam is steered by a remote controlled mirror system into the HERA tunnel where it collides with the electron beam. Back-scattered Compton photons are measured in a position sensitive calorimeter.

Behind the IP, the laser beam hits a mirror attenuator at 0° incidence angle. The reflected power is dissipated into the beam line. The transmitted component is measured by a position sensitive diode after passing through a rotating Glan prism. The dependence of the intensity on the rotation angle is used for measuring the linear component of the laser light after the transport through the mirror system.

3.3 The Calorimeter

The back-scattered Compton photons are detected in a tungsten scintillator sandwich calorimeter which is split into an optically decoupled upper and lower half. To minimize smearing effects, the electron beam optics have been chosen to provide a virtual focus at the position of the calorimeter. The vertical distance of the Compton photons to the center of the calorimeter is obtained from the quantity $\eta = (E_U - E_D)/(E_U + E_D)$. $E_{U(D)}$ is the fraction of the shower energy in the upper (lower) part of the detector.

Figure 11a shows the 2-dimensional distribution of the Compton photon positions η versus their energy $E = E_U + E_D$. The 'bell'-shape is due to the 2-body kinematics of Compton scattering and the non-linear behavior between η and the vertical position. Figure 11b shows the energy projection of the Compton spectrum and of the Bremsstrahlung background.

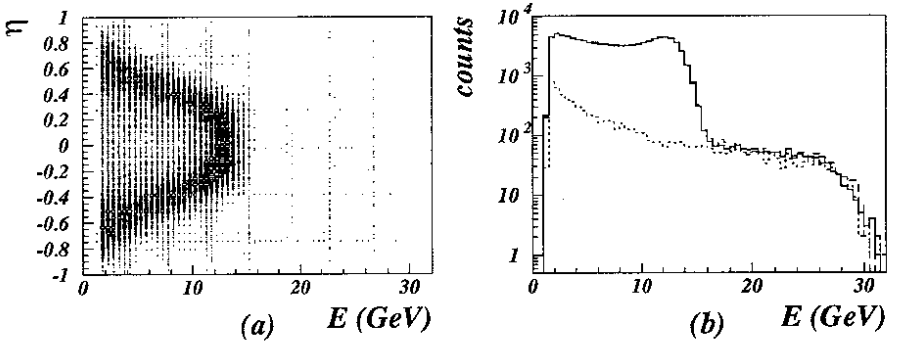

Figure 11: The two-dimensional distribution (position η vs energy) of the back-scattered Compton photons (a) and its one-dimensional energy projection (b) for the two cases that the laser is on resp. off. The Bremsstrahlung background is suppressed by more then a factor of 10 compared to the Compton rate. The Compton edge at 13 GeV is used for the energy calibration of the calorimeter.

3.4 Data Acquisition and Online Analysis

The single photon method requires a fast data acquisition system that is shortly described in the following.

The heart of the online system is a VME card with four 1 MHz 12 bit ADC's and a digital signal processor (DSP)[16]. The four PMT signals are integrated, digitized

and processed with a speed of up to 100 kHz. 2-dimensional histograms, e.g. η vs E and various calibration histograms are filled in real time. The system is triggered either by the discriminated PMT signals alone or in conjunction with the electron bunch timing. Single electron bunches can be selected. Various feed-back systems are programmed that allow a fully automatic operation of the polarimeter: the laser beam can be centered automatically onto the mirror centers and onto the e^--beam. The calorimeter is centered in a feed-back loop onto the center of the Compton beam. During beam injection collimators are closed automatically and calibration data are taken. The optimal PMT voltages are obtained from the measured calibration histograms and the Pockels cell voltage is calibrated using the results from the light analyser.

From the two-dimensional histograms of the DSP, the online program extracts once per minute a background corrected value of the electron polarization. The spin dependence of the Compton cross section is used to extract the transverse and optionally the longitudinal polarization of the electrons and the linear component of the laser light.

In order to check the performance of the polarimeter, linear light can be sent into the tunnel. In this case, the measured asymmetries do not depend on electron polarization. Figure 12a shows the distributions and figure 12c the asymmetries of the Compton photons from horizontal and vertical linear light. They agree well with Monte-Carlo expectations. Figure 12b and d show the results for circular light for an energy range of $E = 5$ to 12 GeV. The fit determined a transverse electron polarization of $P_e = (52.5 \pm 0.6)\%$ and a linear light component of $P_{lin} = (8.1 \pm 0.5)\%$. The results on P_e is quite independent on P_{lin} as the e^- polarization asymmetry is an odd function in η whereas the linear light component is an even function in η. The 'single-photon method' allows fits for various energy bins separately. These separate histograms are all well described by a single Monte-Carlo fit.

Online, the e^- polarization is extracted from the shifts of the means in the η curves (figure 12b). A shift of $\Delta\eta = 0.000908$ corresponds to an electron polarization of $P_e = 1\%$.

The longitudinal component of the electron polarization is derived from the asymmetries of the energy spectrum for right and left circular light. The longitudinal component was always measured to be $P_e^{L_z} \leq 1\%$ at HERA.

Transverse polarization values of up to $P_e = 70\%$ have been observed. The statistical errors are about 1% for a measurement of one minute. The current estimate of the systematic error is $\Delta P_e/P_e \sim 0.1$. It will be reduced drastically in future by calibrating the polarimeter scale using polarization rise time measurements. Figure 13 shows first results of the rise time studies [10].

4 Polarized Internal Gas Targets

An important factor for a precision experiment is a pure target with a high degree of polarization. There is no technology known which would allow one to polarize the nucleons of a pure solid material to a high degree and use them as a target in an electron beam. The only working solution uses mixed materials like ammonium or buthanol in which the hydrogen atoms are polarized whereas the other nucleons stay unpolarized. There are however methods to polarize *pure gases* of H, D, ^3He or other materials to a very high degree without any dilution by other atoms. In addition, the sign of the polarization

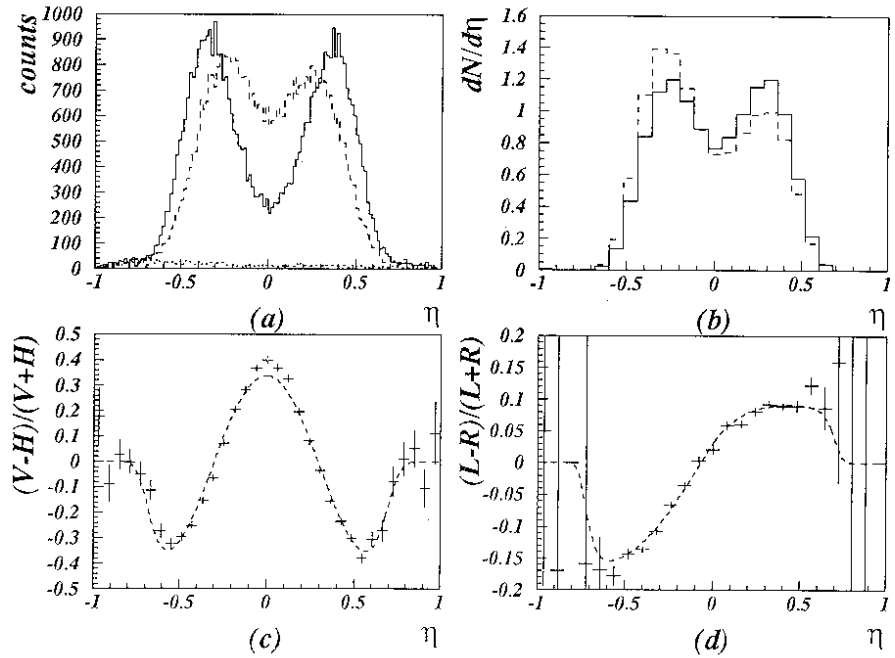

Figure 12: The η-distributions for Compton scattering off horiz. and vert. linear (a) polarized light and right and left circular (b) polarized light and its asymmetries (c) and (d). The lower plots are derived from the upper distributions. The even component of the asymmetry curve is proportional to the linear light asymmetry (c) and the odd one is proportional to the product of circular light polarization and electron polarization (d).

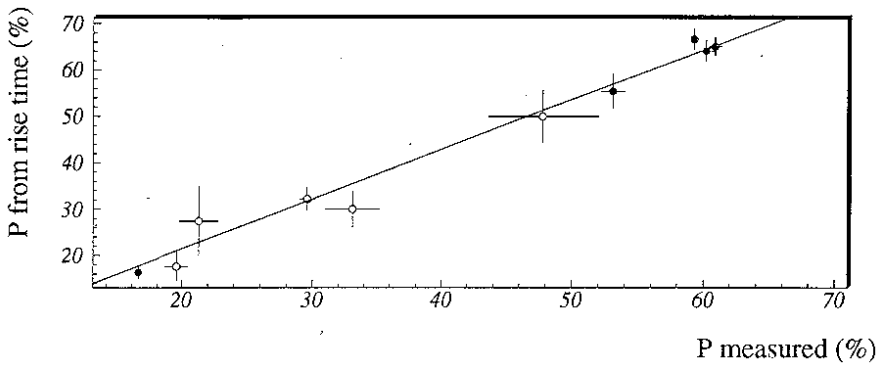

Figure 13: Comparison of the polarization extracted from the rise time constant compared to the measured value in the polarimeter. The two values agree within the statistical and systematic uncertainties.

can be flipped very rapidly. That allows the measurement of asymmetries with small instrumental uncertainties.

Due to the small density of gas targets, external beams are normally not suited as the luminosity is too small. A way around it is to use a high current beam in a storage ring. Using a free gas jet or a cluster jet that crosses the stored beam, the achievable densities are however still far too small to obtain high precision polarization data.

4.1 The Storage Cell – a Novel Technique

This problem has been overcome with the storage cell technique which has been demonstrated for the first time in 1980 when applied at an external beam [17]. As shown in Figure 14 polarized gas atoms are injected from the side into a thin-walled, T-shaped storage cell. The cell acts as an impedance to the polarized gas and increases the target thickness by about two orders of magnitude compared to a free gas jet. The stored beam passes parallel through the center of the tube without interfering with any walls or windows. The chance of interactions of the beam with the gas is magnified by the high number of wall bounces the gas atoms perform before they leave the cell through one of the three openings.

The HERMES storage cell is a $40 \times 3 \times 1$ cm^3 elliptical tube made of pure aluminum with a wall thickness of < 100 μm. The low wall thickness reduces multiple scattering and energy loss of the particles that are scattered through the cell walls.

In case of H and D the cell is coated with drifilm in order to minimize possible depolarization of the atoms during the wall bounces. Another possible depolarization mechanism is resonant depolarization by the electron bunch fields. A homogeneous magnetic field of a strength which is well centered between resonances (e.g. 0.3 T in the case of H and D) suppresses beam induced depolarization.

The cell will be cooled in order to reduce the velocity of the atoms and thus increase

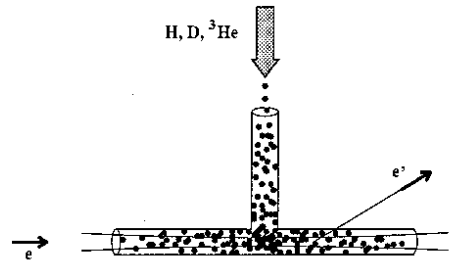

Figure 14: Principle of the storage cell target. The atoms are injected into a T-shaped tube and perform several hundred wall bounces before they leave the cell. This way the thickness of a gas target is increased by two orders of magnitude compared to a free gas jet.

the target thickness. The temperature may however not be too low because then the atoms would stay too long in the storage cell and thus depolarizing mechanisms would become prominent. At HERMES target densities of 10^{14} atoms/cm^2 at 100 K for H and D and $3 \cdot 10^{14}$ atoms/cm^2 at 15 K for ^3He are foreseen.

Figure 15 shows the design of the HERMES target region. A differential pumping system upstream and downstream of the target chamber assures that the vacuum in the ring is not affected by the injected gas. RF-meshes between the storage cell and the beam pipe and at other positions with rapid changes in the cross section of the beam pipe prevent the electron bunches from inducing wake fields and resonant rf losses in the target chamber which could heat up and destroy the storage cell.

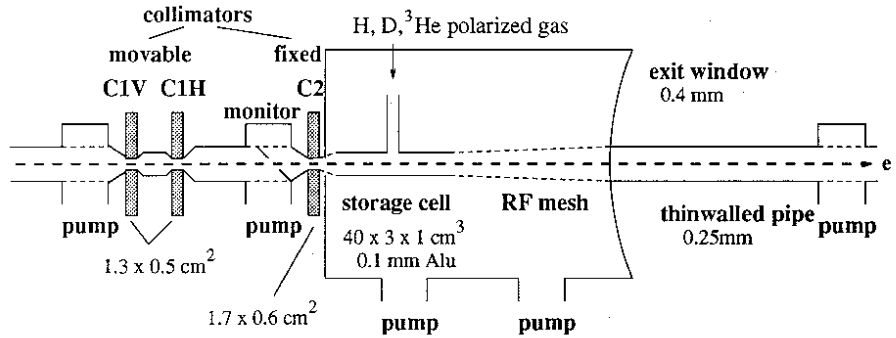

Figure 15: Simplified sketch of the HERMES target region. The storage cell is protected against radiation by a collimator system. RF-meshes protect from electromagnetic fields. Large pumps keep the vacuum conditions good despite of the target gas leaking out of the storage cell.

4.2 Beam Collimators – an Essential to Storage Cell Targets

Beam collimators in front of the storage cell are essential at HERA for two reasons: the beam has tails and the beam is accompanied by synchrotron radiation.

The profile of an electron beam is essentially gaussian, however there are large non-gaussian tails e.g. due to beam-restgas interactions. As the storage cell has to be small in order to keep the gas density high, the cell walls can easily enter the region of the beam tails. Even if the tails are only very slightly populated, the scattering rate from the wall material easily dominates the rate from the gas scattering as the wall density is many orders of magnitude larger than the gas density. The collimators have to be thick (e.g. 10 cm tungsten) in order to be able to absorb the shower produced by high energy beam particles.

A second and even more important reason for having a collimator system is synchrotron radiation, which has effects on the operation of the storage cell and the detector:

- The storage cell is heated by synchrotron radiation. The heating leads to a reduction of the target density by temperature rise and in extreme cases to a destruction of the thin cell walls. The HERMES cell with no shielding is heated by about 100 W.
- The wall-coating of the cell may be destroyed by photon irradiation, causing a stronger wall depolarization of the polarized target gas. The unshielded HERMES cell is irradiated by about 10^{16} photons per second.
- Synchrotron radiation is scattered off the target gas, the walls of the storage cell, the collimator edges and the vacuum pipe. The main scattering processes are Compton scattering, Rayleigh scattering and the photoelectric effect with subsequent fluorescence light emission. The scattered radiation enters the front part of the HERMES detector and prevents the operation of the wire chambers unless counter-measures are taken.

In order to reduce the synchrotron radiation generated in the HERA dipole magnets, the straight section in front of the target was enlarged from 5.8 m to 140 m. Secondly the last bending section in front of the straight section is split into a strong bending part and an additional weak magnet. By this means the power density at the target is reduced from $P/\Delta x = 150$ W/mm to $P/\Delta x = 1.5$ W/mm and the characteristic energy is reduced by a factor of 5 to $E_c = 15$ keV. Thus the dipole radiation can be shielded more easily.

A method to reduce quadrupole radiation is to weaken the quadrupoles in the straight section and to place them at a larger distance from the target. The β-functions in the quadrupoles should also be decreased. These requirements are in conflict with the necessary focusing of the beam at the target and with the global HERA beam requirements. Therefore this method is not applicable for the HERMES experiment.

A very efficient way of reducing the remaining synchrotron radiation is a collimator system as described in the following.

- A movable horizontal and vertical collimator C_{1H} and C_{1V} with an opening of $\pm 6.5 \times 2.6$ mm^2 placed about 2 m upstream the target shields the subsequent collimator and the storage cell from direct synchrotron radiation.

- A fixed elliptical collimator C_2 located close to the target with an aperture of $\pm 8.6 \times 3.0$ mm^2 in the shadow of C_{1H} and C_{1V} shields the storage cell from radiation that is edge-scattered at C_1.

With this arrangement only double scattered radiation may hit the detector and the storage cell. An exception is the radiation scattered at the gas which cannot be shielded.

A detailed simulation of the synchrotron radiation was performed [18] and gave confidence that the synchrotron radiation can be shielded without causing any problems to the HERMES detector.

4.3 Test of Storage Cell Targets

Test at TSR (Heidelberg)

A storage cell target using the same polarized beam source as foreseen for the HERMES experiment has been tested at the Test Storage Ring in Heidelberg [19]. A stored 27 MeV α-beam was scattered off polarized hydrogen atoms in the storage cell target. Figure 16 shows the measured spin asymmetry of the process $\vec{p} + \alpha \rightarrow \vec{p} + \alpha$. This picture reflects the beauty of the method: The upper measurement was taken in an external α-beam. The measurement is dominated by the background from the beam halo scattered off the cell walls. The lower measurement was taken in a storage ring. Hardly any background is visible. The pure, highly polarized gas atoms give large experimental asymmetries.

Figure 17 shows the polarization and the density of the gas in the cell as function of the cell temperature. The density increases with decreasing temperatures as expected. Only at low temperatures below 100 K a significant depolarization of the gas can be observed.

Test at HERA

The HERMES storage cell was installed in the HERA ring in spring '94 together with the collimator system and a set of detectors that allowed us to measure the background conditions. A gas feed system was used to inject H_2, ^3He and N_2 with arbitrary density, however unpolarized only.

The test of the storage cell target was a complete success:

- The lifetime of the electron beam was reduced by the target gas as expected.
- High energy particles scattered off the target gas could be observed.
- The synchrotron radiation was reduced efficiently by closing the movable collimators.
- The closure of the collimators did not reduce the lifetime of the beam nor did it produce high additional shower background.
- There was no heating of the storage cell, either by synchrotron radiation or by rf heating.

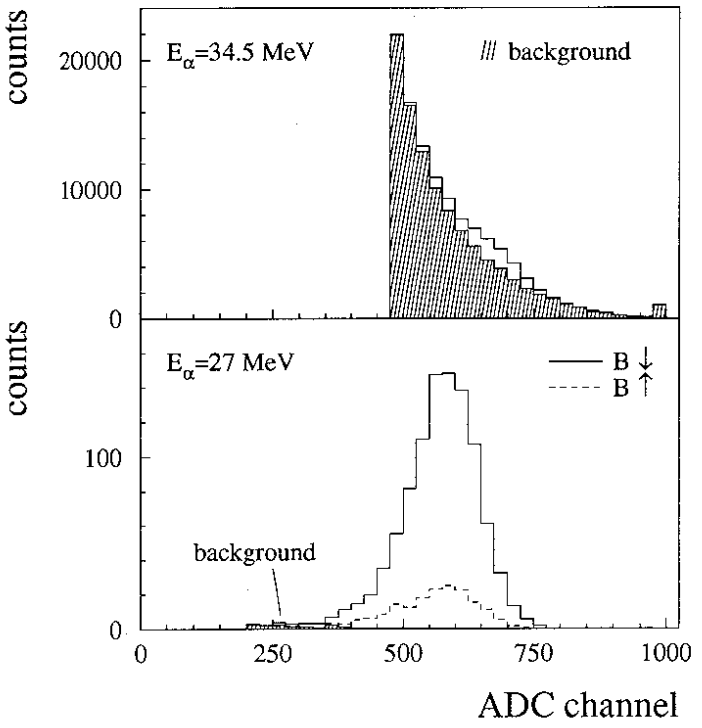

Figure 16: The same storage cell target was used once in an external beam and once in a storage ring. Large background is observed in the external beam (upper plot). Small background and large spin asymmetries are observed at the TSR storage ring in Heidelberg (lower plot).

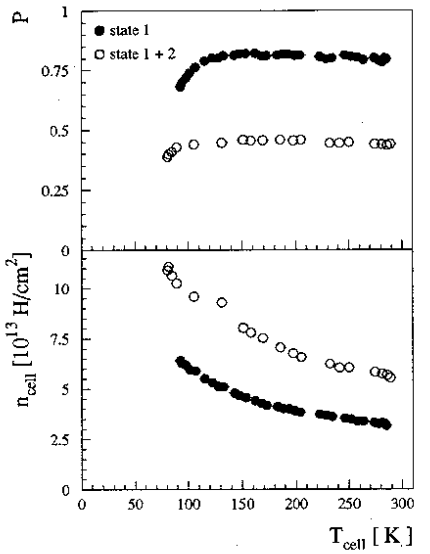

Figure 17: Polarization and density of the gas in the storage cell as a function of cell temperature. The polarization drops only at very low temperatures (upper plot) due to wall depolarization. The target density is higher at low temperatures as the atoms need more time to leave the storage cell (lower plot).

4.4 Polarized Gas Sources

Two different types of polarized gas sources will be used at HERMES:

- an atomic beam source for hydrogen and deuterium
- and a laser-driven source for ^3He.

Atomic Beam Source

The presently most intense polarized atomic beam source has been build at Heidelberg [20]. It is based on the Stern-Gerlach separation of atomic hydrogen or deuterium and functions as follows (see figure 18):

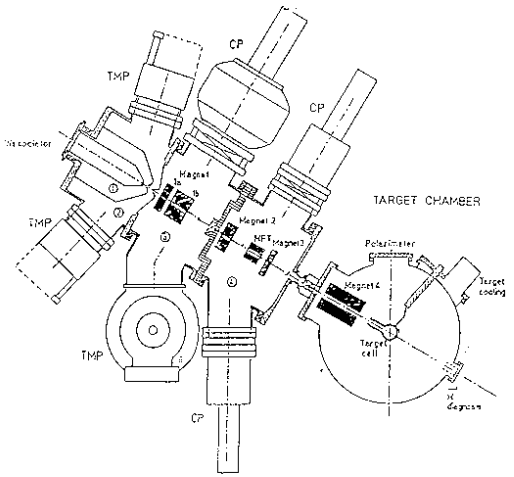

Figure 18: Sketch of the polarized atomic beam source as used for the measurements at the TSR in Heidelberg.

Molecular H (resp. D) is dissociated by rf discharge into H (resp. D) atoms and a beam is formed by a cooled nozzle and skimmers. The atomic beam is fed through a system of sextupole magnets. Depending on the state of the electron spin of the atom, the beam particle is focused or defocused. For efficient separation of the spin states, strong permanent magnets with pole tip fields of 1.5 T are used. For the remaining two hyperfine substates rf-transitions are induced in a way, that the proton spins become aligned.

The source produces an atomic beam with an intensity of $8 \cdot 10^{16}$atoms/sec in two hyperfine states and with a polarization of better than 90%.

^{3}Helium Source

The ^3He source [21] is based on a completely different physical principle: By electrical discharge a small fraction of helium atoms in a pumping cell is converted into a metastable state (2^3S_1). Circularly polarized laser light of high intensity incident on the metastable atoms excites transitions in the atoms and thus transfers angular momentum to the metastable atoms. The metastable atoms become polarized. Metastability exchange collisions transfer the polarization to the ground state atoms.

The ^3He source is able to deliver high intensities (e.g. $2 \cdot 10^{17}$ atoms/s) however the polarization is currently only on the order of 50–60%. It has been successfully operated as a storage cell target at the medium energy proton storage ring at IUCF [22].

5 The HERMES Detector

Although the HERMES detector [1] is not really subject of this report, the basic features of the detector will be shortly outlined in order to show the capabilities of the HERMES experiment:

The detector, as shown in figure 19 is a standard spectrometer. It consists of an open dipole magnet with a field strength of $\int B\,dl = 1.5$ Tm with field clamps that reduce the stray field. The proton and electron beam pipes go through the center of the magnet and are shielded against magnetic field by a septum plate.

Upstream of the magnet a system of μ-strip gas counters and drift chambers is used to determine the vertex position and the angle of the scattered particles. The drift chambers behind the magnet are used to determine the momentum of the particle after its bending in the spectrometer field. Additional proportional chambers in the magnet simplify the track recognition.

The projected resolution of the kinematical variables are $\Delta Q^2/Q^2 < 1.5\%$ and $\Delta x/x = 1 - 8\%$ where Q^2 is the 4-momentum transfer and x is the Bjørken scaling variable. The resolution of the system is not limited by the chamber resolution but by the multiple scattering and energy loss of the particles in the target wall materials.

A lead glass calorimeter in combination with a preshower wall and a hodoscope wall allow for an efficient trigger of the data acquisition system on high energy electrons. An energy threshold of about 3.5 GeV will reject most of the pion background. A TRD is used in combination with the lead glass calorimeter to further suppress pion background and to unambiguously identify electrons and positrons from hadrons. A threshold Cerenkov counter will separate pions from kaon and proton signals. This allows HERMES to do semi-inclusive pion physics. At a later stage it is planned to replace the threshold counter by a ring image Cerenkov to unambiguously identify kaons and protons.

Luminosity will be monitored by a separate Møller (Bhabha) detector that measures the scattering of the $e^-(e^+)$-beam off the electrons of the target gas atoms.

The HERMES detector has almost full acceptance within the kinematical limits:

$$\begin{aligned} E_{beam} &= 27.5\ GeV \\ 0.02 < x &< 0.8 \\ Q^2 &> 1\ GeV^2 \end{aligned}$$

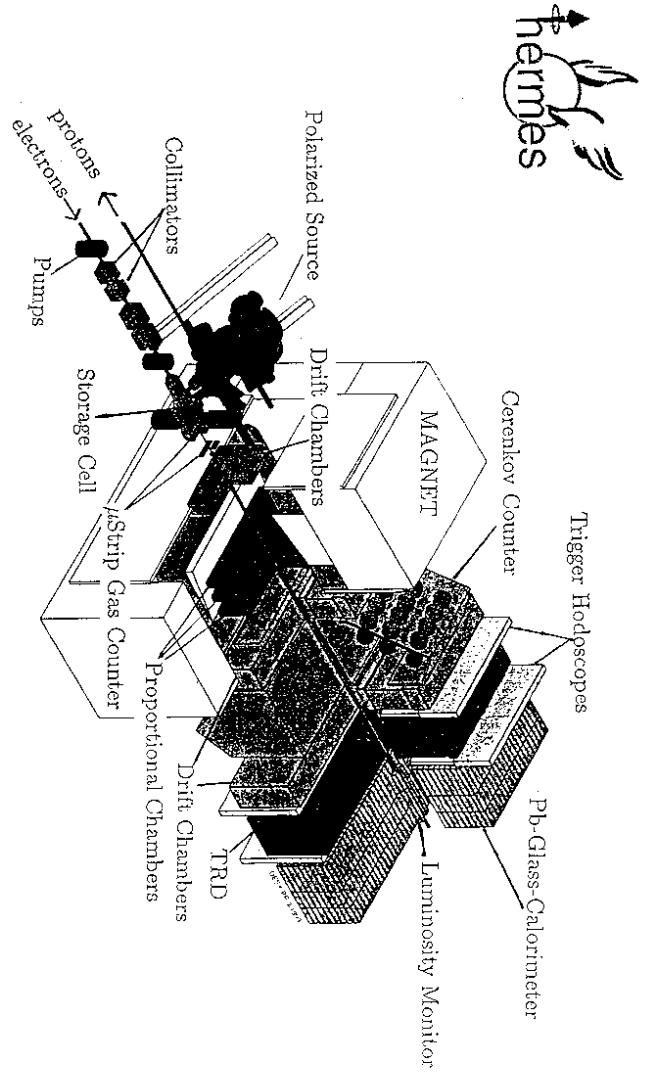

Figure 19: The HERMES detector.

$$\begin{aligned} W &> 2\ GeV \\ y &< 0.85 \\ 40\ mrad < \theta &< 250\ mrad \end{aligned} \tag{8}$$

with Q^2 and x as defined above, θ and E' being the angle and energy of the scattered electron, $\nu = E_{beam} - E'$ and $y = \nu/E_{beam}$ are the absolute and relative energy transfer to the virtual photon, and W is the invariant mass of the hadronic final state. The cut on y will reduce radiative corrections. The cuts on W and Q^2 will select deep inelastic events outside the resonance region. The data in the resonance region ($W < 2$ GeV) will be used for a special analysis. Figure 20 shows the kinematical region that is accessible by the HERMES experiment.

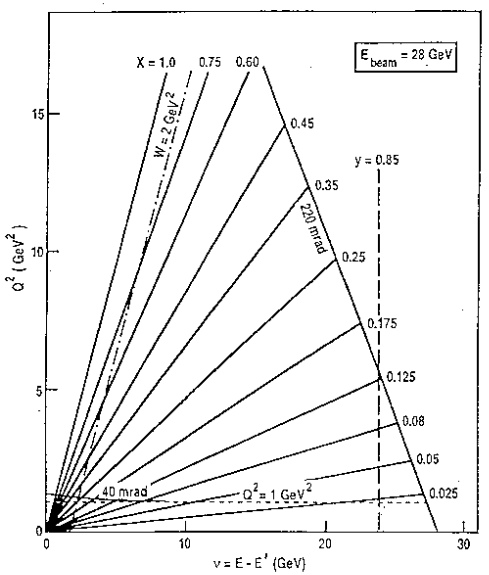

Figure 20: The kinematical plane accessible by HERMES. The W, Q^2 and y cuts are indicated as dashed lines. The quantity ν is the energy loss of the beam electron.

6 Design Criteria of Spin Experiments

The main physics goal of the on-going spin experiments at CERN, SLAC and the future experiment at DESY is the understanding of the spin structure of proton and neutron. How well the experiments can fulfill this goal depends on the following criteria:

- the completeness of experimental information,
- the statistical precision
- and the systematic precision.

6.1 Completeness

A complete experimental investigation of the spin structure of the nucleon includes the following items:

- measurement of deep inelastic scattering processes with longitudinally polarized beams and polarized targets;
- proton and neutron target (H and D or ^3He);
- longitudinal and transverse target polarization;
- tensor polarization in the case of spin-1 targets (D);
- x and Q^2 distributions;
- registration and reconstruction of complete events;
- flavor tagging by identification of the hadronic final state;
- identification of photons from radiative processes;
- coverage of the full kinematic area especially in x for sum rules;
- results from different beam energies (resp. significantly different Q^2 ranges).

6.2 Statistical Precision

The statistical precision can approximately be expressed in the following figure of merit F:

$$F = \rho\, t\, I\, (p_B\, p_T\, f)^2 \tag{9}$$

with ρ being the target density, t the total running time, I the averaged beam current, p_B the average beam polarization, p_T the average target polarization and f the dilution factor.

The dilution factor f, which is the number of polarizable nucleons, makes the crucial difference in precision in the comparison of gas targets with $f^2 \sim 1$ and solid targets with $f^2 \sim 0.018$ (in the case of buthanol).

In the case of a small dilution and high beam and target polarization the observed asymmetry is large in regions where the spin asymmetry of the physics process is large. In this case (which applies to HERMES) the statistical error is even smaller than expected from equation (9) due to an extra term in the formula for the error calculation.

6.3 Systematic Precision

The systematic precision of a spin experiment is mainly determined by the following criteria:

- *rapid polarization reversal without acceptance changes:* not the precision of the absolute measurement counts but the precision of the asymmetry measurement;
- *no dilution, high polarization:* the larger the observed asymmetry is, the smaller are the relative errors;
- *good beam and target polarimetry;*
- *thin targets, no additional material:* low radiation length, no target windows;
- *low background.*

The concept of the HERMES experiment is to cover as many of the above design criteria as possible.

7 The Physics Goals

The goal of the spin experiments is to understand the spin structure of matter i.e. to test theories and models that describe the dynamics of the quarks and gluons in the nucleon [1][23]. More explicitly it means experimentally isolating the quark spin distributions

$$\delta q_f(x, Q^2) = q_f^+(x, Q^2) - q_f^-(x, Q^2) \tag{10}$$

in the kinematic variables x and Q^2 for the different quark flavors f. Here q_f^+ (q_f^-) denotes the fraction of the quark distribution function coming from quarks with spin parallel (antiparallel) to the nucleon spin.

Additionally the integrated spin contributions of the quark flavors

$$\Delta q_f(Q^2) = \int_0^1 \delta q_f(x, Q^2)\, dx \tag{11}$$

are of special interest together with the fraction of the spin carried by gluons ΔG and by angular momentum L_z. The total spin of the nucleon adds up to $s_z^N = 1/2$, so the following equation holds for the sum of the various contributions:

$$s_z^N = \frac{1}{2} = \frac{1}{2}\,(\Delta u_v + \Delta d_v + \Delta q_s) + \Delta G + L_z \tag{12}$$

Beyond the above basic quark spin distributions, there are additional spin structure functions that describe transverse spin distributions of quarks and spin distributions in nuclear targets.

Theory predicts several spin sum rules that can be tested by experiment. The most fundamental sum rule is the Bjørken sum rule which relates the spin structure functions to the axial current coupling known from beta-decay. An experimental failure of the Bjørken sum rule would cause severe problems to our basic understanding of the nucleon in terms of the parton model. Assuming its validity, the Bjørken sum rule can be used to precisely determine the value of the QCD coupling constant $\alpha_s(Q^2)$.

8 Inclusive Spin Physics at HERMES, SMC and SLAC

8.1 Cross Sections and Asymmetries

The spin-dependent part of the polarized deep inelastic cross section is given by the following formula [24]:

$$\frac{d^3(\sigma(\alpha)-\sigma(\pi+\alpha))}{dx\,dy\,d\Phi} = \frac{e^4}{4\pi^2 Q^2}\left[\cos\alpha\left(\left[1-\frac{y}{2}-\frac{y^2}{4}\gamma^2\right]g_1(x,Q^2)-\frac{y}{2}\gamma^2 g_2(x,Q^2)\right)\right.$$
$$\left.-\sin\alpha\cos\Phi\sqrt{\gamma^2\left[1-y-\frac{y^2}{4}\gamma^2\right]}\left(\frac{y}{2}g_1(x,Q^2)+g_2(x,Q^2)\right)\right]. \quad (13)$$

The kinematic variables are defined as usual: $\nu = E - E'$, $x = Q^2/2M\nu$, $y = \nu/E$ and $\gamma = \sqrt{Q^2}/\nu$. α is the polar angle of the target polarization vector with respect to the beam direction and Φ is the azimuthal angle with respect to the lepton scattering plane.

According to this formula the determination of the spin structure functions $g_1(x)$ and $g_2(x)$ requires a combined asymmetry measurement off a longitudinally and a transversely polarized target. Because of the mixing of g_1 and g_2 a precise determination of g_1 from a longitudinally polarized target alone is not possible.

The experimentally measured cross section asymmetries $A_\parallel$ and $A_\perp$:

$$A_\parallel = \frac{\sigma^{\uparrow\downarrow}-\sigma^{\uparrow\uparrow}}{\sigma^{\uparrow\downarrow}+\sigma^{\uparrow\uparrow}}; \qquad A_\perp = \frac{\sigma^{\uparrow\leftarrow}-\sigma^{\uparrow\rightarrow}}{\sigma^{\uparrow\leftarrow}+\sigma^{\uparrow\rightarrow}} \quad (14)$$

obtained by spin flip of a longitudinally and transversely polarized target can be related to the asymmetries A_1 and A_2 of the exchanged virtual photon by the relations

$$A_\parallel = D\cdot(A_1+\eta\cdot A_2) \quad \text{and} \quad (15)$$
$$A_\perp = d\cdot(A_2-\xi\cdot A_1). \quad (16)$$

The kinematic factors D, d and η, ξ are defined by

$$D = \frac{y(2-y)}{y^2+2(1-y)(1+R)} \quad (17)$$
$$\eta = \frac{2\gamma(1-y)}{(2-y)} \quad (18)$$
$$d = D\sqrt{\frac{2\epsilon}{1+\epsilon}} \quad (19)$$
$$\xi = \eta\frac{1+\epsilon}{2\epsilon} \quad (20)$$

with $\epsilon = (1-y)/(1-y+y^2/2)$ being the degree of transverse polarization of the virtual photon. D and d can be regarded as depolarization factors of the virtual photon. $R = R(x,Q^2)$ is the ratio of cross-sections for longitudinally and transversely polarized virtual photons.

In contrast to the measured asymmetries $A_\parallel$ and $A_\perp$, the virtual photon asymmetries A_1 and A_2 do not depend on the beam energy E or y and are directly related to the photon absorption cross section of the nucleon for a given x and Q^2:

$$A_1 = \frac{\sigma_{1/2}-\sigma_{3/2}}{\sigma_{1/2}+\sigma_{3/2}} = \frac{g_1-\gamma^2 g_2}{F_1} \quad (21)$$
$$A_2 = \frac{\sigma_{TL}}{\sigma_T} = \frac{\gamma(g_1+g_2)}{F_1} \quad (22)$$

Here $\sigma_{(1/2)}$ ($\sigma_{(3/2)}$) is the virtual photoabsorption cross section when the projection of the total angular momentum of the photon-nucleon system along the incident lepton direction is 1/2 (3/2), $\sigma_T = 1/2(\sigma_{(1/2)}+\sigma_{(3/2)})$ is the total transverse photoabsorption cross section and σ_{TL} is a term arising from the interference between transverse and longitudinal amplitudes.

8.2 The Spin Structure Function $g_1(x)$ of Proton and Neutron

The spin structure function $g_1(x)$ has a direct interpretation in terms of quark spin distributions:

$$g_1(x,Q^2) = \frac{1}{2}\left[\frac{4}{9}\delta u(x)+\frac{1}{9}\delta d(x)+\frac{1}{9}\delta s(x)+\frac{4}{9}\delta\bar{u}(x)+\ldots\right] \quad (23)$$

where $\delta u(x) = u^+(x) - u^-(x)$ and $u^+(x)$ ($u^-(x)$) are the momentum distributions of u-quark with spin parallel (anti-parallel) to the nucleon spin.

There are data available on $g_1^p(x)$ of the proton from EMC [26], SMC [27] and E143 [29]. Figure 21 show the latest data from E143 and SMC for the asymmetry $A_1(x) \approx g_1/F_1$.

The experimental information on $g_1^n(x)$ of the neutron is a lot less precise. First data were taken by SMC [28], E142 [30] and E143 [31]. The neutron structure function is experimentally extracted by two methods: It is firstly derived from the comparison of deuteron and hydrogen targets and secondly from ^3He. In ^3He the spins of the two protons are mostly antiparallel so that ^3He can be regarded as an approximate neutron target. The asymmetries are however diluted by the protons and additionally small nuclear corrections have to be applied to correct for the p-wave component of the nuclear wave function. Figure 22 show the latest data on $g_1^n(x)$.

8.3 The Spin Structure Function $g_2(x)$

A precise determination of g_1 requires a measurement of $g_2(x)$ because of the mixing of g_1 and g_2 in equation (13). The determination of $g_2(x)$ has however also a physical interest in its own. $g_2(x)$ is needed to construct and distinguish between several models of the nucleon. Additionally $g_2(x)$ is sensitive to quark gluon correlations that appear as twist-3 operators in the operator product expansion [24]:

$$g_2(x) = -g_1(x) + \int_x^1 g_1(x')\frac{dx'}{x'} + \tilde{g}_2(x). \quad (24)$$

Different approaches predict that either $\tilde{g}_2(x)$ is zero (Wandzura-Wilczek relation) or, if twist-2 and twist-3 components cancel, $g_2(x)$ is zero. $g_2(x)$ is in any case limited by the

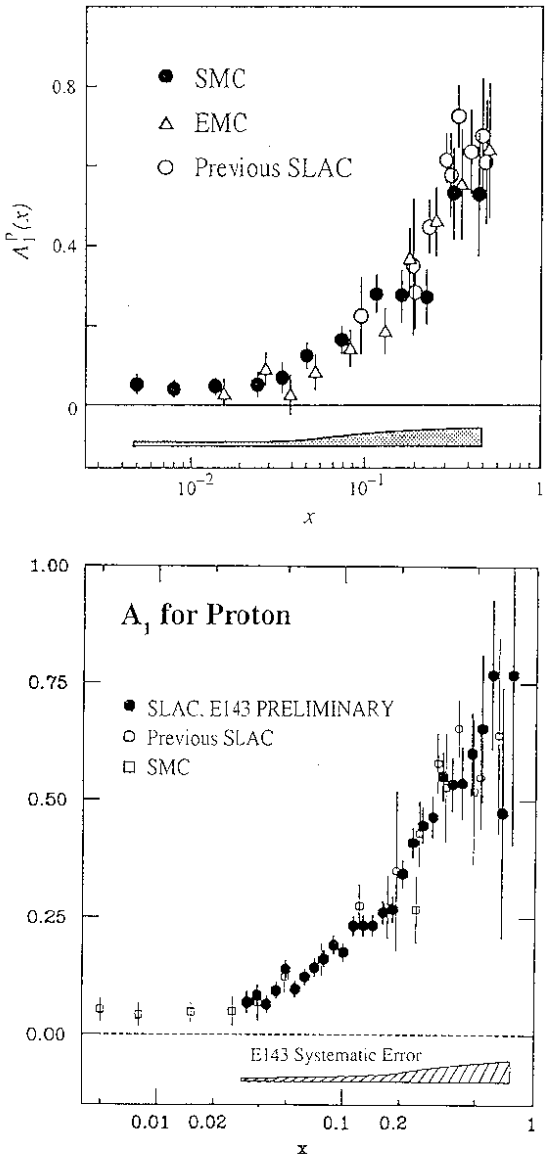

Figure 21: World data on the spin asymmetry $A_1^p(x) = g_1(x)/F_1(x)$ of the proton. The upper plot shows the original EMC data, the old SLAC and the new SMC data. The lower plot shows the SMC data together with recent SLAC data. The new data confirm the EMC measurement that lead to the spin-crisis. The new SLAC data are very precise at medium x. The main interest in the SMC data are the low x points which might indicate an unexpected large contribution in the Ellis Jaffe integral coming from the low x extrapolation.

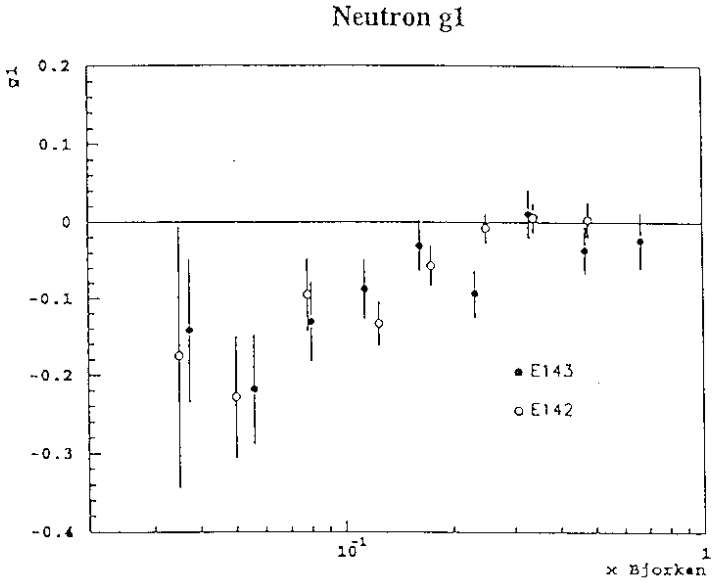

Figure 22: The spin structure function $g_1^n(x)$ of the neutron as measured at SLAC. New, precise data from SLAC and HERMES are expected soon.

relation $A_2 < \sqrt{R}$. First data from SMC [33] indicate that A_2^p is small compared to $\sqrt{R}$. Figure 23 shows a model of $g_2(x)$ [34] and the anticipated precision of the HERMES data.

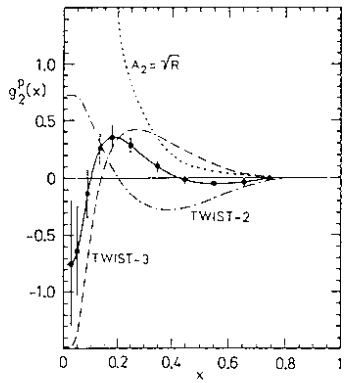

Figure 23: A model of $g_2(x)$ and projected errors bars for a standard 800 h HERMES run with transverse polarized hydrogen at a target density of 10^{14} nucleons/cm^2.

8.4 The Sum Rules and the Determination of α_s

Besides the shape of the various structure functions, their integrals allow important tests of different models and basic assumptions about the spin structure of the nucleon.

Ellis Jaffe Sum Rule

The Ellis Jaffe sum rule [25], derived from SU(3)$_f$ symmetry arguments, was experimentally found to be violated [26]:

$$\int_0^1 g_1^p(x)\,dx = (0.189)_{theor} = (0.126 \pm 0.010 \pm 0.015)_{EMC/SLAC}\,. \qquad (25)$$

This result caused the so-called *'spin crisis'* in 1987: hundreds of theoretical papers were written that tried to explain the failure by different models and new experiments were proposed to check the experimental result. The violation of the Ellis Jaffe sum rule was experimentally confirmed lately by results from SLAC and SMC for the proton and also for the neutron. Today, the violation of the Ellis Jaffe sum rules is explained by the fact that one of the assumptions needed for the derivation of the sum rule does not apply: The spin contribution of the nucleon coming from the strange sea seems to be much higher than originally expected. Additionally the Q^2 evolution of the QCD corrections seem to play an important role. Table 1 shows the latest (preliminary) results on the sum rules from

EMC [26], SMC [27],[28] and SLAC [29]–[32]. The data sets are basically all consistent. Small deviations can be explained by the use of different unpolarized input structure functions (EMC) and by the Q^2 dependence of the higher order QCD corrections. A major experimental limitation on the precision of the sum rules comes from the model dependent extrapolation of the structure functions towards $x \to 0$.

Table 1: Results of the Ellis Jaffe and the Bjørken Sum Rules.

Ellis-Jaffe (proton):

experiment (target)	result	theory	$\langle Q^2 \rangle$
EMC (NH_3)	$0.126 \pm .010 \pm .015$	$0.189 \pm .005$	10 GeV^2
SMC (C_4H_9OH)	$0.136 \pm .011 \pm .011$	$0.176 \pm .006$	10 GeV^2
E143 (NH_3)	$0.129 \pm .004 \pm .009$	$0.160 \pm .006$	3 GeV^2

Ellis-Jaffe (deuteron):

experiment (target)	result	theory	$\langle Q^2 \rangle$
SMC (C_4D_9OD)	$0.023 \pm .020 \pm .015$	$0.085 \pm .005$	4.6 GeV^2
E143 (ND_3)	$0.044 \pm .003 \pm .004$	$0.068 \pm .004$	3 GeV^2

Ellis-Jaffe (neutron):

experiment (target)	result	theory	$\langle Q^2 \rangle$
SMC (C_4D_9OD) & EMC (NH_3)	$-0.08 \pm .04 \pm .04$	$0.002 \pm .005$	4.6 GeV^2
E142 (^3He)	$-0.022 \pm .007 \pm .009$	$-0.021 \pm .018$	2 GeV^2

Bjørken:

experiment (targets)	result	theory	$\langle Q^2 \rangle$
SMC (C_4D_9OD) & EMC (NH_3)	$0.20 \pm .05 \pm .04$	$0.191 \pm .002$	4.6 GeV^2
SMC (C_4H_9OH) & SMC (C_4D_9OD) & E142 (^3He)	$0.163 \pm .017$	$0.185 \pm .004$	5 GeV^2
E142 (^3He) & EMC (NH_3)	$0.146 \pm .021$	$0.183 \pm .007$	2 GeV^2
E143 (NH_3) & E142 (^3He)	$0.151 \pm .014$	$0.171 \pm .008$	3 GeV^2

Bjørken Sum Rule

The Bjorken sum rule [36]:

$$\int_0^1 [g_1^p(x) - g_1^n(x)]\,dx = \frac{1}{6}\left|\frac{g_A}{g_V}\right| + \text{QCD corr.} \qquad (26)$$

relates the structure functions $g_1^{p,n}$ to the axial charges g_A and g_V measured in Gamov-Teller nuclear β-decay. A violation of the Bjorken sum rule would cast doubt on the validity of the quark model or pertubative QCD. First results from SLAC (see table 1) and SMC confirm the Bjørken sum rule on the 1-σ level with a precision of about 10%. More precise data will come from the HERMES experiment.

The Quark Spin Content of the Nucleus

Using the results for the Ellis-Jaffe integrals for proton and neutron, and additionally some $SU(3)_f$ symmetry arguments, the spin fraction which is carried by the u, d and s

quarks in the nucleon can be determined separately [35]:

$$\int_0^1 g_1^{p(n)}(x)\,dx \;=\; \frac{1}{12}\left(\pm a_3 + \frac{a_8}{3}\right) + \frac{1}{9}\Delta q + \text{QCD corr.} \qquad (27)$$

with

$$a_3 = g_a/g_v = F + D = \Delta u - \Delta d \quad \text{(known from neutron decay)}, \qquad (28)$$
$$a_8 = 3F - D = \Delta u + \Delta d - 2\Delta s \quad \text{(known from hyperon decay)}, \qquad (29)$$
$$a_0 = \Delta q = \Delta u + \Delta d + \Delta s \quad \text{(total spin carried by quarks)}, \qquad (30)$$

and $F = 0.459 \pm 0.008$; $D = 0.798 \pm 0.008$. Using QCD corrections to third order, the following results were obtained from the SMC and SLAC data quoted at a renormalization scale $Q^2 = 10\ GeV^2$ [37]:

$$\Delta u = 0.83 \pm .03, \quad \Delta d = -0.43 \pm .03, \quad \Delta s = -0.10 \pm .03, \quad \Delta q = 0.31 \pm .07 \qquad (31)$$

QCD evolution makes the results Q^2 dependent. At SLAC energies about 1/3 of the nucleon spin is carried by the quarks. The rest of the spin must be carried by gluons or angular momentum. The strange sea Δs has a significant contribution.

Determination of α_s

The dependence of the Bjørken sum rule on QCD corrections allows the extraction of the strong coupling constant $\alpha_s(Q^2)$ once the validity of the sum rule is accepted [37]:

$$\int_0^1 [g_1^p(x) - g_1^n(x)]\,dx \;=\; \frac{1}{6}\left|\frac{g_A}{g_V}\right|\left[1 - \left(\frac{\alpha_s(Q^2)}{\pi}\right) - 3.5833\left(\frac{\alpha_s(Q^2)}{\pi}\right)^2 - 20.2153\left(\frac{\alpha_s(Q^2)}{\pi}\right)^3 - O(130)\left(\frac{\alpha_s(Q^2)}{\pi}\right)^4 + \ldots\right] \qquad (32)$$

$\alpha_s(Q^2)$ as extracted from spin structure functions can be compared with the value extracted from high energy jet physics. An agreement of those values would be (another) convincing proof of the universal validity of QCD as theory of hadronic interactions. A first analysis of the SLAC data with QCD corrections to 4^{th} order gave a value of [37]:

$$\alpha_s(2.5\ GeV^2) = 0.375^{+0.062}_{-0.081} \qquad (33)$$

corresponding to:

$$\alpha_s(M_z^2) = 0.122^{+0.005}_{-0.009}. \qquad (34)$$

This is in agreement with the results from LEP: $\alpha_s(M_z^2) = 0.117 \pm .005$. The advantage of the results from the Bjørken sum rule are that they can be taken with decreasing energies and as such confirm the running coupling behavior, i.e. the Q^2-dependence of QCD results at low energies.

Burkhardt-Cottingham Sum Rule

The Burkhardt-Cottingham sum rule [38]

$$\int_0^1 g_2(x)\,dx = 0 \qquad (35)$$

is less fundamental, but its violation would rule out certain classes of spin models of the nucleon [24]. Higher moments

$$\int_0^1 x^n g_2(x, Q^2)\,dx \qquad (36)$$

are interesting because they test results from QCD operator product expansion which are model independent [34].

8.5 The Q^2-Dependences and Resonance Production

The Q^2-dependence of the spin structure functions is interesting for several reasons: First of all the sum rule integrals require data over x at fixed Q^2. As however the data of all existing experiments have different mean Q^2 values at different x, the data have to be corrected which is only possible when the Q^2-dependence is known. Secondly, the Q^2 evolution of the spin structure functions can be calculated by QCD. A verification would be an important test of QCD.

HERMES will study the Q^2 dependence of the spin structure funtions and also the spin dependence of resonance production at $Q^2 > 1$.

8.6 Tensor Spin Observables

As the deuteron is a spin-1 target there exist two higher multipole structure functions called $b_1(x)$ and $\Delta(x)$. The functions can be measured by scattering an unpolarized beam off a longitudinally tensor-polarized or transversely polarized target respectively. Both functions are expected to be small.

The knowledge of the structure function $b_1(x)$ is required for a precise derivation of $g_1^n(x)$ and $g_2^n(x)$ from deuterium. A non-zero $b_1(x)$ would indicate that the quark distributions of the nucleons change due to nuclear binding effects.

$\Delta(x)$ has a similar interpretation. It probes gluon components which are not assigned to individual nucleons within the nucleus [24].

9 Semi-Inclusive Spin Physics Program of HERMES

The only direct way to separate the spin content of the different quark flavors are semi-inclusive hadron measurements. The scattered lepton is measured in coincidence with the leading hadrons. The quark kinematics (x and Q^2) is extracted from the scattered lepton kinematic (Θ and E') while at the same time the flavor of the quark is determined by identifying the type of the leading hadron in the current jet. This kind of flavor tagging works only statistically and requires the knowledge of the fragmentation functions.

However results of EMC [39] have shown that it works well when the right cuts are applied, mainly a cut on the fractional energy z

$$z = E_h/\nu \tag{37}$$

with E_h being the energy of the hadron. Table 2 shows the number of hadrons expected in a 800 h run of the HERMES experiment. A Monte-Carlo program PEPSI [40] has been

Table 2: Expected statistics of hadrons for different cuts on the hadronic energy z. The table was calculated for a 800 h HERMES run at 35 GeV with a target density of 10^{14} nucleons/cm^2 of hydrogen.

z-cut	>0.0	>0.1	>0.6	>0.8
γ	1125,000	466,000	154,000	–
π^+	582,000	468,000	48,000	13,500
π^-	430,000	313,000	27,000	6,300
K^+	66,000	63,000	18,000	7,500
K^-	44,000	38,000	4,100	1,200

developed to simulate the hadron production in polarized deep inelastic scattering. It is based on the string fragmentation programs LEPTO and JETSET of the Lund group [41].

9.1 Flavor Decomposition of Valence Distributions

The most important and direct method of quark flavor decomposition makes use of the spin asymmetries $A_\pi(x)$ of the pion charge differences. It requires a longitudinally polarized beam and a longitudinally polarized target and tags on identified positive and negative pions at high z. Only the charge difference $N^{\pi^+-\pi^-} = N^{\pi^+} - N^{\pi^-}$ is used in the analysis which ensures that effects from the (charge symmetric) sea and from resonance and vector meson decays cancel to a large extend. It can be shown that in the measured pion asymmetry

$$A_\pi(x) = \frac{N^{\pi^+-\pi^-}_{\uparrow\downarrow} - N^{\pi^+-\pi^-}_{\uparrow\uparrow}}{N^{\pi^+-\pi^-}_{\uparrow\downarrow} + N^{\pi^+-\pi^-}_{\uparrow\uparrow}} \tag{38}$$

all fragmentation effects cancel if one assumes that the fragmentation process factorizes from the quark scattering process and is independent of the helicity of the quarks. In this case $A_\pi(x)$ of proton and deuteron can be directly related to the spin asymmetries of the valence quark distributions u_v and d_v [42]:

$$A^p_\pi(x) = \frac{4\delta u_v(x) - \delta d_v(x)}{4u_v(x) - d_v(x)} \qquad A^d_\pi(x) = \frac{\delta u_v(x) - \delta d_v(x)}{u_v(x) - d_v(x)} \tag{39}$$

As the unpolarized flavors distributions u_v and d_v are known, the above equations allow to extract the spin distributions δu_v and δd_v separately and as a function of x. Figure 24 shows the projected precision of the HERMES experiment for δu_v and δd_v using two different structure function models as input for the PEPSI program [42].

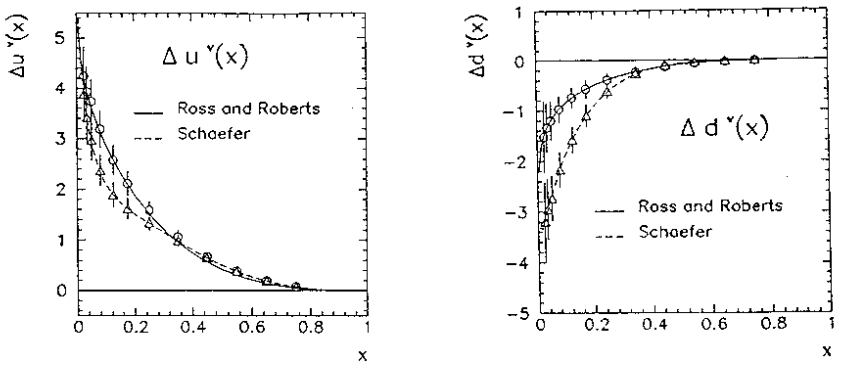

Figure 24: Projected precision of the HERMES experiment for δu_v and δd_v. The results were obtained with the PEPSI Monte-Carlo using input spin distributions from models of Ross and Roberts and from Schäfer for a standard 800 h HERMES run with polarized hydrogen and deuterium at a target density of 10^{14} atoms/cm^2.

Sea Contribution to Nucleon Spin

Using one spin structure function (e.g. of deuterium) in addition to the semi-inclusive results and assuming some average charge of the sea $\langle e_s^2 \rangle$, in principle the sea contributions $\delta q_s(x)$ can also be extracted using the following formula:

$$g_1^d(x) = \frac{5}{18}\,\delta u_v(x) + \frac{5}{18}\,\delta d_v(x) + \langle e_s^2 \rangle\,\delta q_s(x). \tag{40}$$

Integral Valence Contributions

The integral valence contributions can be calculated from the semi-inclusive results

$$\Delta u_v = \int_0^1 \delta u_v(x)\,dx \tag{41}$$

$$\Delta d_v = \int_0^1 \delta d_v(x)\,dx \tag{42}$$

$$\Delta q_s = \int_0^1 \delta q_s(x)\,dx \tag{43}$$

and can be compared to the results obtained from the Ellis-Jaffe integrals by SU(3) arguments (eqs. (27) – (refeqej2)) and also applied to the basic formula

$$\frac{1}{2}\left[\Delta u_v + \Delta d_v + \Delta q_s\right] + \Delta G + L_z = \frac{1}{2}. \tag{44}$$

The projected precision for a standard HERMES run of 800 h with hydrogen and deuterium at a target density of 10^{14} atoms/cm^2 is shown in table 3.

Table 3: Expected statistical and systematical errors for the valence spin contributions.

	statist.	extrapol.	unpol.
Δu_v	0.06	0.10	0.10
Δd_v	0.09	0.06	0.06

9.2 Strange Sea Contribution to the Nucleon Spin

The *strange* sea contribution $\delta s(x)$ can be directly measured by tagging leading K^- mesons at high z and low x. As the K^- meson consists of $(s\bar{u})$ quarks, leading K^- mesons originate mostly in fragmentation from s-quarks (to some extend also from $\bar{u}$-quarks) from the sea. $K^+ = (u\bar{s})$ mesons are not useful for this kind of analysis as they are dominated by fragmentation of valence-u quarks. Figure 25 shows some predictions of K^- asymmetries

$$A_{K^-}(x) = \frac{N^{K^-}_{\uparrow\downarrow} - N^{K^-}_{\uparrow\uparrow}}{N^{K^-}_{\uparrow\downarrow} + N^{K^-}_{\uparrow\uparrow}} \tag{45}$$

generated by the PEPSI Monte-Carlo program. The kaon spin analysis requires the knowledge of the fragmentation functions of u, d and s quarks into kaons.

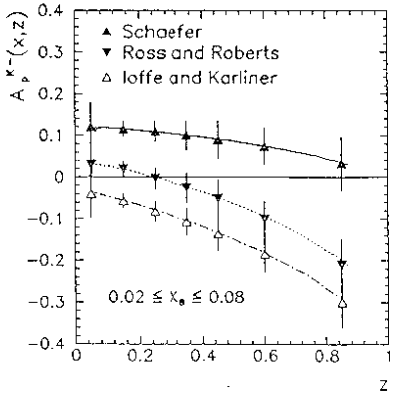

Figure 25: Predictions of K^- asymmetries for HERMES as a function of the kaon energy for different models of spin structure functions (standard 800 h run).

9.3 Tensor Charge of the Nucleon

Recently it has been discovered that there is a leading twist, chiral-odd structure function $h_1(x)$ that can in principle be measured in deep inelastic scattering [43]. As the function is leading twist, it is a fundamental quantity which does not disappear at high energies. The function is connected to a helicity flip amplitude of the transverse spin components of

the quarks (transversity). Therefore a transverse polarized target is required. It can not be directly measured in inclusive processes, however h_1 is connected to pion asymmetries $A(x,z)$ in the current fragmentation region by the formula

$$A(x,z) = A_k(Q^2)\frac{\Sigma_a e_a^2[h_1^a(x)\hat{e}^a(x) + \hat{f}_1^a(z)xg_T(x)]}{\Sigma_a e_a^2 f_1^a(x)\hat{f}_1^a(z)}. \tag{46}$$

$\hat{f}_1^a(z)$ is the quark fragmentation function for flavor a obtained from unpolarized semi-inclusive scattering, $\hat{e}_1^a(z)$ is a new chiral-odd fragmentation function, $g_T = g_1 + g_2$ and $A_k(Q^2)$ is a kinematical factor. It is currently not clear how well $h_1(x)$ can be experimentally disentangled from the fragmentation effects.

9.4 Angular Momentum Contribution to the Nucleon Spin

There is a method to directly identify angular momentum of quarks in the nucleon [44]: Using an unpolarized beam on a transversely polarized target, rotating constituents produce an azimuthal asymmetry of the hadrons. The asymmetry is periodic with $\phi = \pi$, i.e. the azimuthal distribution has two maxima and two minima and can this way be distinguished from other spin effects which have a period of $\phi = 2\pi$. It is however not completely clear how to derive quantitatively out of the measured asymmetries the total angular momentum of the constituents.

9.5 Gluon Contributions

A direct way to extract gluonic contributions in deep inelastic scattering is the observation of spin asymmetries of high-p_t jets or J/Ψ production in the gluon fusion process. Due to the relatively low energies at HERMES, those processes are suppressed and will probably not be statistically significant.

An alternative method to observe the possibly large anomalous gluon contribution [45] in polarized nucleon scattering uses semi-inclusive asymmetries of charged, leading ($z > z_m = 0.2$) pions of a longitudinally polarized proton target [46]:

$$A^p_{\pi^+ + \pi^-} = \frac{N^{\pi^+ + \pi^-}_{\uparrow\downarrow} - N^{\pi^+ + \pi^-}_{\uparrow\uparrow}}{N^{\pi^+ + \pi^-}_{\uparrow\downarrow} + N^{\pi^+ + \pi^-}_{\uparrow\uparrow}} \tag{47}$$

The semi-inclusive asymmetry $A^p_{\pi^+ + \pi^-}(x, z_m)$ can be compared to the inclusive asymmetry $A_1^p(x)$. The difference depends on the strange spin content $\Delta s(x)$ and on the anomalous gluon contribution $\Delta\Gamma$:

$$\begin{aligned} A^p_{\pi^+ + \pi^-}(x, z_m) - A_1^p(x) &= s(x)\,\frac{a(z_m)}{18F_1(x)}\,\frac{g_1(x)}{F_1(x)} \\ &- \Delta s(x)\,\frac{a(z_m)}{18F_1(x)} \\ &+ \Delta\Gamma\,\frac{(\alpha_s/2\pi)}{18F_1(x)}\,[6(1-\lambda) + \lambda a(z_m)] \end{aligned} \tag{48}$$

with

$$a(z_m) = \frac{\int_{z_m}^{1} [z/(z+1)] D(z)\, dz}{\int_{z_m}^{1} [1/(z+1)] D(z)\, dz} \tag{49}$$

and $D(z)$ being a fragmentation function. The analysis requires certain symmetries of the fragmentation process (spin independence, charge and isospin invariance). λ is an unknown parameter which has to be determined experimentally. It accounts for the unknown fragmentation behavior of events generated by the gluon anomaly. Details can be found in ref. [46].

10 Unpolarized Physics Program of HERMES

It should be mentioned that the HERMES storage cell target can be filled with any *unpolarized* gas at any density, limited only by beam lifetime considerations. Asymmetries between different gas types can be measured by a rapid change of the gas. There is a long list of interesting unpolarized measurements which can be done [1]. Two are listed here:

- determination of the flavor asymmetry $\bar{d} > \bar{u}$ of the quark sea by measuring the isospin distribution of pions $(N^{p\pi^-} - N^{n\pi^-})/(N^{p\pi^+} - N^{n\pi^+})$
- precision measurement of the valence flavour distribution d_v/u_v by looking at charge asymmetries $N^{\pi^+} - N^{\pi^-}$

11 Conclusions

Spin physics is a rich field that has gained a boost of interest during the *spin crisis* which was induced by the surprising results from EMC in 1987. Since then large progress has been made theoretically, and also experimentally with the recent results from SMC and SLAC. Precise and more complete experimental information is expected soon from the HERMES experiment at DESY.

HERMES utilizes new experimental technologies, namely a *polarized storage cell target inside a polarized storage ring.* The art of polarizing the HERA electron machine has already now reached a status which is well above the requirements for the HERMES experiment.

References

[1] HERMES Collaboration, K. Coulter et al., *Proposal* DESY-PRC 90/01, (1990);
HERMES Collaboration, *Technical Design Report*, DESY-PRC 93/06 (1993)
also:
M. Düren, K. Rith, *Polarized Electron Nucleon Scattering at HERA: the HERMES experiment.*, Proc. of Physics at HERA, Vol. 1, eds. W. Buchmüller and G. Ingelman, Hamburg, DESY, Oct. 1991, p. 427.

[2] D.P. Barber et al., DESY report, DESY 94-171 (1994).

[3] D.P. Barber et al., Nucl. Instr. Meth. **A329** (1993) 79;
M. Düren, *The HERA Polarimeter*, Proc. of 10^{th} Int. Symp. of High Energy Spin Physics, Nov. 1992, Nagoya, eds. T. Hasegawa et al. (Univ. Acad. Press, Tokyo, 1993) p. 911.

[4] M. Böge, *Analysis of Spin Depolarizing Effects in Electron Storage Rings*, Ph.D. Thesis, Univ. of Hamburg, 1994, DESY 94-087 (1994).

[5] A.A. Sokolov and I.M. Ternov, Sov. Phys. Doklady **8** (1964) 1203.

[6] V. Bargman, L. Michel and V. Telegdi, Phys. Rev. Lett. **2** (1959) 435.

[7] D.P. Barber, *Theory and Observation of Electron Polarization in High Energy Storage Rings*, Proc. of 10^{th} Int. Symp. of High Energy Spin Physics, Nov. 1992, Nagoya; eds. T.Hasegawa et al. (Univ. Acad. Press, Tokyo, 1993) p. 83.

[8] D.P. Barber et al., Nucl. Instr. Meth. **A338** (1994) 166.

[9] M. Böge, *Optimization of Spin Polarization in the HERA Electron Ring using Beam-Based Alignment Procedures*, Proc. of 11^{th} Int. Symp. of High Energy Spin Physics, Sep. 15-22, 1994, Bloomington, in preparation.

[10] C. Grosshauser, Diploma thesis, Univ. Erlangen-Nürnberg, 1994, DESY-HERMES 94-01 (1994).

[11] D.P. Barber, *Spin Depolarization in Storage Rings*, Proc. of 11^{th} Int. Symp. of High Energy Spin Physics, Sep. 15-22, 1994, Bloomington, in preparation.

[12] J. Buon and K. Steffen, Nucl. Instr. Meth. **A245** (1986) 248.

[13] D.P. Barber et al., Part. Accel. **17** (1985) 243.

[14] T. Sloan, Lancaster Univ., private communication (1994).

[15] E. Gianfelice-Wendt and M. Böge, *Polarization Studies for HERA-e in Presence of Spin Rotators*, p. 915 in ref. [7].

[16] A. Caldwell et al., ZEUS Note 92-022 (1992).

[17] M.D. Barker et al., *Polarization Phenomena in Nuclear Physics* eds. G.G.Ohlsen et al., AIP, New York, (1981), 931.

[18] M. Düren, *Protecting the HERMES Experiment from Synchrotron Radiation*, Proc. of 9^{th} Int. Symp. of High Energy Spin Physics, Sept. 1990, Bonn; eds. W. Meyer et al., (Springer-Verlag, Berlin, 1991) Vol. 2, p. 217

[19] K. Zapfe et al, *A High Density Polarized Hydrogen Gas Target for Storage Rings*, accepted for publication in Rev. Sci. Instrum. (Jan. 1995)

[20] F. Stock et al., Nucl. Instr. Meth. **A343** (1994) 334.

[21] K. Lee et al., Nucl. Instr. Meth. **A333** (1993) 294.

[22] K. Lee et al., Phys. Rev. Lett. **70** (1993) 738.

[23] review articles and references therein e.g.:
A. Manohar, Proc. Polar. Coll. Worksh., Univ. Park USA (1990) 90;
F. Close, this volume;
B.L. Ioffe and M. Karlinger, SLAC-PUB-5235 (1990);
G. Altarelli and G.G. Ross, Phys. Lett. **212B** (1988) 391.

[24] R.L. Jaffe, Colloque de Physique **C6** (1990) 149.

[25] J. Ellis and R.L. Jaffe, Phys. Rev. **D9** (1974) 1444, **D10** (1974) 1669.

[26] EMC, J.Ashman et al., Phys. Lett. **206B** (1988), Nucl. Phys. **B328** (1989) 1.

[27] SMC, D. Adams et al., Phys. Lett. **B329** (1994) 399.

[28] SMC, B. Adeva et al., Phys. Lett. **B302** (1993) 533.

[29] E143, K. Abe et al., SLAC preprint, SLAC-PUB-6508 (1994), subm. to Phys. Rev. Lett.

[30] E142, P.L. Anthony et al., Phys. Rev. Lett. **71** (1993) 959.

[31] J. McCarthy, contrib. to 27^{th} Int. Conf. on High Energy Physics, Glasgow, July 1994

[32] E143, H. Borel, contrib. to 11^{th} Int. Symp. of High Energy Spin Physics, Sep. 15-22, 1994, Bloomington

[33] SMC, Phys. Lett. **B336** (1994) 125.

[34] A. Schäfer and L. Mankiewicz, *The Polarized Structure Function* $g_2(x)$., Proc. of Physics at HERA, Vol. 1, eds. W. Buchmüller and G. Ingelman, Hamburg, DESY, Oct. 1991, p. 411.

[35] F.E. Close and R.G. Roberts, Phys. Lett. **B165** (1993) .

[36] J.D. Bjorken, Phys. Rev. **148** (1966) 1457, **D1** (1970) 1367.

[37] J. Ellis, M. Karliner, CERN Preprint, CERN-TH-7324/94

[38] G.H. Burkhardt et al., Ann. Phys. (NY) **56** (1970) 453.

[39] T. Sloan et al., Phys. Reports **162** (1988) 45.

[40] L. Mankiewicz et al., *PEPSI 1.1*, Proc. of Physics at HERA, Vol. 3, eds. W. Buchmüller and G. Ingelman, Hamburg, DESY, (Oct. 1991) p. 1395.

[41] T. Sjöstrand, Comp. Phys. Comm. **39** (1986) 347.

[42] M. Veltri et al., *Polarized Quark Distributions from Semi-Inclusive Leptoproduction* Proc. of Physics at HERA, Vol. 1, eds. W. Buchmüller and G. Ingelman, Hamburg, DESY, (Oct. 1991) p. 447.

[43] R.L. Jaffe and X. Ji, Phys. Rev. Lett. **67** (1991) 552.

[44] T.C. Meng, Proc. XXIV Renc. de Moriond, Les Arcs (1989) 287.

[45] G. Altarelli and G.G. Ross, Phys. Lett. **B212** (1988) 391.

[46] St. Güllenstern et al., Phys. Lett. **B312** (1993) 166-172.

Contents

1 Introduction 1

2 Polarized Beams in Storage Rings 2
- 2.1 Polarization in High Energy Storage Rings . . . 2
- 2.2 Optimization of Transverse Polarization . . . 3
- 2.3 RF-Depolarization and Energy Calibration . . . 4
- 2.4 The HERA Spin Rotators . . . 6
- 2.5 Longitudinal Electron Polarization . . . 8
- 2.6 Polarization during Luminosity Conditions . . . 10
- 2.7 Spin Tracking MC-Program . . . 10
- 2.8 Polarized Protons at HERA . . . 11

3 Beam Polarimeters 12
- 3.1 The HERA Compton Polarimeter . . . 12
- 3.2 The Laser Optics . . . 13
- 3.3 The Calorimeter . . . 14
- 3.4 Data Acquisition and Online Analysis . . . 14

4 Polarized Internal Gas Targets 15
- 4.1 The Storage Cell – a Novel Technique . . . 17
- 4.2 Beam Collimators – an Essential to Storage Cell Targets . . . 19
- 4.3 Test of Storage Cell Targets . . . 20
- 4.4 Polarized Gas Sources . . . 23

5 The HERMES Detector 24

6 Design Criteria of Spin Experiments 26
- 6.1 Completeness . . . 27
- 6.2 Statistical Precision . . . 27
- 6.3 Systematic Precision . . . 28

7 The Physics Goals 28

8 Inclusive Spin Physics at HERMES, SMC and SLAC 29
- 8.1 Cross Sections and Asymmetries . . . 29
- 8.2 The Spin Structure Function $g_1(x)$ of Proton and Neutron . . . 30
- 8.3 The Spin Structure Function $g_2(x)$ . . . 30
- 8.4 The Sum Rules and the Determination of α_s . . . 33
- 8.5 The Q^2-Dependences and Resonance Production . . . 36
- 8.6 Tensor Spin Observables . . . 36

9 Semi-Inclusive Spin Physics Program of HERMES 36
- 9.1 Flavor Decomposition of Valence Distributions . . . 37
- 9.2 Strange Sea Contribution to the Nucleon Spin . . . 39
- 9.3 Tensor Charge of the Nucleon . . . 39

- 9.4 Angular Momentum Contribution to the Nucleon Spin . . . 40
- 9.5 Gluon Contributions . . . 40

10 Unpolarized Physics Program of HERMES 41

11 Conclusions 41

[33]. E. Witten, Phys.Lett.105B (1981) 267 ;
L.E. Ibáñez and G.G. Ross, Phys.Lett. 110B (1982) 227.

[34]. H.P. Nilles, M. Srednicki and D. Wyler, Phys. Lett. 124B (1983) 337.

[35]. H. Georgi, unpublished (1974) ;
H. Fritzsch and P. Minkowski, Ann. Phys. 93 (1975) 193 ;
H. Georgi and D.V. Nanopoulos, Nucl. Phys. B155 (1979) 59.

[36]. R. Cahn, L. Hall and I. Hinchliffe, Phys. Lett. 109B (1982) 426.

[37]. S. Dimopoulos, private communication.

[38]. F. Del Aguila, J.M. Moreno and M. Quiros, preprint CERN-TH.5616/90 (1990).